Water Attachment onto Size-Selected Cationic Pyrene Clusters

Sébastien Zamith, Ali Kassem, Jean-Marc L'Hermite, Christine Joblin

Water Attachment Onto Size-Selected Cationic Pyrene Clusters

Sébastien Zamith,[*,†] Ali Kassem,[†,‡] Jean-Marc L'Hermite,[†] and Christine Joblin[‡]

†*Laboratoire Collision Agrégats Réactivité (LCAR/IRSAMC), UMR5589, Université de Toulouse III - Paul Sabatier and CNRS, 118 Route de Narbonne, F-31062 Toulouse, France*

‡*Institut de Recherche en Astrophysique et Planétologie (IRAP), UMR5277, Université de Toulouse III - Paul Sabatier, CNRS, CNES, 9 avenue du Colonel Roche, F-31028 Toulouse, France*

E-mail: sebastien.zamith@irsamc.ups-tlse.fr

Abstract

We report measurements of the attachment rates of water molecules onto mass-selected cationic pyrene clusters for size from n=4 to 13 pyrene units and for different collision energies. Comparison of the attachment rates with the collision rates measured in collision induced dissociation experiments provides access to the values of the sticking coefficient. The strong dependence of the attachment rates on size and collision energy is rationalized through a model in which we use a Langevin-type collision rate and adjust on experimental data the statistical dissociation rate of the water molecule from the cluster after attachment. This allows us to extrapolate our results to the conditions of isolation and long time scales encountered in astrophysical environments.

1 Introduction

Polycyclic aromatic hydrocarbons (PAHs) are major products in combustion processes[1,2] and their clusters could be involved in soot formation. Schuetz and Frenklach suggested the role of the pyrene ($C_{16}H_{10}$) dimer but this proposal has been challenged by low temperature laboratory experiments.[3] More recently, Mercier et al.[4] performed fluorescence emission measurements in flames and reported spectroscopic evidence for the presence of PAH dimers and their role in soot nucleation. They concluded that the nucleation process is controlled by kinetics rather than thermodynamics.

In another context, PAHs are major constituents of astrophysical environments and the presence of PAH clusters has been proposed to explain some of the features associated with mid-infrared spectral observations. PAH clusters were initially proposed to explain the broad bands associated with the aromatic infrared bands (AIBs) in the 3-14 μm range.[5] AIBs result from radiative cooling of PAHs following the absorption of UV photons from stars and are therefore particularly bright in regions of massive star formation.[6] Analysis of AIB spectral maps in these regions has shown that different populations emit with relative abundances depending on local physical conditions, in particular the UV photon flux. PAH cations are localized in the most exposed regions, while a population of evaporating very small grains (eVSGs) is observed in the more protected regions.[7–9] Furthermore, the analysis showed that free (neutral) PAHs are produced by the destruction of eVSGs during UV photoprocessing. This led to consider PAH clusters as good analogues of these eVSGs and motivated the study of their physical and chemical properties. Modeling results showed that PAH clusters are very short-lived in UV-irradiated environments and are therefore likely transported from deeper inside dark molecular clouds into the UV-irradiated regions where IR emission is observed.[10,11]

In the dense and cold astrophysical environments found in molecular clouds, but also in prestellar condensations and protoplanetary disks, gas-grain interactions lead to the formation of molecular ices and promote chemical reactions that cannot occur in the gas phase

at very low temperatures. These processes have important consequences, notably on the formation of complex organic molecules and the appearance of snow lines that define the transitions from gas to solid form for the most important volatile molecules (e.g. H_2O, CO, CO_2). These snow lines have an impact on the conditions and efficiency of planet formation.[12–15] One of the parameters to be considered in gas-grain chemical models concerns a realistic description of the dust populations involved. These include a variety of materials, mainly carbon and silicate rich, and a size distribution ranging from a few tenths of a micrometer, or more in some regions, to nanometer sizes or smaller. The smallest sizes include eVSGs and PAHs, but the latter appear to be primarily localized in UV-irradiated regions, as discussed above. Small grains can provide a large surface area for reactivity. They can also undergo large temperature spikes upon cosmic ray collisions or photon absorption and could thus contribute significantly to the molecular enrichment of the gas phase. Gas-grain interactions involving (very) small grains could thus play a key role in the evolution of physical and chemical conditions in the cold phases of star formation and in protoplanetary disks.[16–19]

One of the topics in laboratory astrophysics concerns the characterization of gas-grain interactions for relevant laboratory analogues of interstellar dust. In a recent review, Potapov and McCoustra[20] emphasized the need for quantum chemical experiments and calculations to overcome the classical view of dust-ice mixing in which a refractory dust core is surrounded by a thick mantle of ice. This classical picture corresponds to most experiments, which are performed on extended surfaces focusing on molecular ices. In these experiments, the ices are deposited on substrates that are suitable for diagnosis (e.g., KBr windows for IR spectroscopy) but are not analogues of interstellar dust. Recent experiments in which the ices have been mixed with carbonaceous and silicate grains with sizes of tens to hundreds of nanometers have demonstrated the impact of dust on several processes such as the desorption kinetics of H_2O[21] or the sticking probability of H_2O.[22]

In this paper, we consider the interaction of H_2O molecules with isolated PAH clusters, and more specifically with mass-selected cationic pyrene clusters. The experimental method

is described in Section 2. In Section 3, we present the values of the water attachment rate for different cluster sizes (n=4-13 pyrene units) and different collision energies. We then estimated the collision rates to derive values for the sticking coefficient. The variation of the attachment rate with cluster size and collision energy is discussed in more detail in section 4 by comparison with a model that includes a Langevin-type collision rate and statistical dissociation. This allows us to extrapolate the results to isolated conditions in astrophysical environments. We conclude in Section 5.

2 Experimental Methods

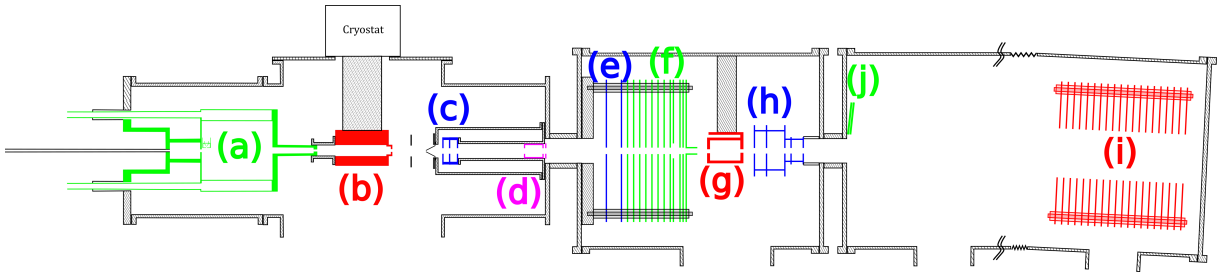

Figure 1: Schematic view of the experimental setup. (a) Cluster gas aggregation source. (b) Thermalization chamber. (c) First stage of Wiley-McLaren acceleration. (d) Mass filter. (e) Energy focusing. (f) Deceleration. (g) Collision cell. (h) Second stage of Wiley-McLaren acceleration. (i) Reflectron. (j) Microchannel plate detector.

2.1 Experimental Setup

Collisions between mass-selected pyrene clusters and water molecules are performed using the experimental setup sketched in Figure 1. In the following, we briefly present the principle of operation of the experimental setup. If necessary, additional details can be found elsewhere.[23,24] Clusters are produced in a gas aggregation source (a) described previously.[24] The oven is filled with a small amount (a few milligrams) of pyrene powder (purity 98%, Aldrich). Typically, the oven temperature is controlled around 40 °C to obtain the optimal

vapor pressure of pyrene. The double-walled source is cooled by a liquid nitrogen circulation. A controlled flow of helium gas is introduced into the source through the furnace. The typical pressure of the source is estimated to be about 1 mbar. Ions are created in the source, at the outlet of the furnace, by electron ionization. The electrons are emitted by a tungsten filament maintained at -150 V and heated by a current of about 2.4 A. Upon electron ionization, ionization and dissociative ionization can occur. We do observe a fraction of slightly dehydrogenated cations (-H, -2H). In addition, minor fragments involving carbon loss ($C_{n=1-4}H_3$) are present, indicating a contribution from rather energetic events.[25–28] Depending on the source conditions, cluster size distributions centered on a few pyrene units up to a few tens of pyrene units can be produced.

After their production, the clusters are carried by the helium flow to the chamber (b) maintained at 25 K. The helium pressure in this chamber is about 1 mbar. There, thousands of collisions with helium ensure the thermalization of the clusters at 25 K. At the exit of the thermalization chamber, an electrostatic spatial focusing is used to optimize the transmission of the ions through a 1 mm diameter skimmer to the high vacuum part of the setup. There are two different mode of operation: in the first mode, the mass spectra of all species formed in the source are recorded over the whole mass range; in the second mode, clusters of a given mass are selected and their kinetic energy is strongly reduced, then they undergo collisions with water molecules and finally the products of the collision are mass discriminated and detected.

In the first mode of operation, we use only the first Wiley-McLaren accelerator stage (c) and the reflectron (i). Clusters are detected using dual microchannel plates (MCP) (j) biased at -10 kV. This mode is used to perform regular time-of-flight mass spectrometry (TOF-MS) in order, for example, to optimize cluster production. In this mode, the mass filter (d), the energy focusing (e) and deceleration (f) electrodes, as well as the second Wiley-McLaren accelerator stage (h), are grounded.

In the second mode of operation, all electrodes are used to mass select clusters. In order

to perform low-energy collisions between the mass-selected clusters and water molecules, precisely delayed high-voltage pulses are applied to electrodes (c), (d), (e), and (f). The pulsed high voltages applied to the first Wiley-McLaren electrodes (c) accelerate all clusters to an average kinetic energy of 622 ± 103 eV. Approximately 26 cm downstream of this first acceleration, there is a linear (at first-order) relationship between the position of the clusters and their kinetic energy. By applying a pulsed high voltage at the right time, we create in this region (e) an electric field which compensates this linear dispersion of kinetic energy. At the exit of the region (e), the clusters of the mass of interest all have the same kinetic energy to within a few eV. In the following, this drastic reduction of the kinetic energy dispersion is called "energy focusing". Due to the time of application of this pulsed high voltage, only the mass of interest is properly focused in energy and will have the proper final kinetic energy. After this focusing of the kinetic energy, the ions are decelerated by an electrostatic potential barrier (f). At the end of the potential barrier, the potential is turned off during the time the clusters pass through a field-free zone and the mass-selected clusters then fly freely through the collision cell (the cell length is L_{cell}=5 cm)(g) to the second Wiley-McLaren acceleration stage (h). The clusters are then analyzed in mass with the reflectron (i) and detected by the MCP detector (j). A high voltage is applied to the mass filter (d) as the mass of interest enters the cylinder and is cut off before it exits. This eliminates some of the neighboring masses.

The kinetic energy distributions of the ions are determined by well-controlled experimental parameters. For example, the distances in the experimental setup are well known, and the time delays between voltage pulses are precisely controlled, as are the voltages. Therefore, by measuring the time it takes for the ions to travel from the end of the slowing down stage to the second acceleration stage, the velocity of the ions is obtained. By recording the signal of the ions as a function of time delays and/or voltages, a precise calibration of the kinetic energy can be obtained. By simulating the ion trajectories, these signals can be reproduced and the kinetic energy distribution of the ions can be obtained.[23]

2.2 Collisions

Once mass-selected and slowed down, the clusters fly through the collision cell. This cell is 5 cm long with an inner diameter of 2.5 cm. Cluster ions enter the cell through a 5 mm diameter hole while the exit hole has a diameter of 6 mm. Two 1 cm diameter tubes are attached to the side of the cell. One is used to introduce the gas or molecular vapor while the other is connected to two pressure gauges. We measure the pressure in the cell simultaneously with an ionization gauge and a capacitive gauge. While the capacitive gauge is useful for obtaining absolute values of pressure, the ionization gauge is used to record pressure because it is more stable under our experimental conditions. We determined that the calibration factor to be applied to the ionization gauge value is 0.8 for water and 2.35 for xenon.

The effective length of the cell is considered to be the same as its physical length. Indeed, numerical simulations have shown that for similar collision cell designs, the pressure leakage out of the cell is almost entirely compensated by the pressure decrease inside the cell close to the apertures.[29]

The kinetic energy of the cluster in the laboratory frame was varied from 5 to 20 eV in 5 eV steps for the water attachment experiment. High collision energy dissociation was performed using xenon and a constant center-of-mass (COM) collision energy of 10 eV, leading to kinetic energies in the laboratory frame ranging from 100 to 206 eV, for cluster sizes of n=6 to 13, respectively. The kinetic energy distributions have a total width at half maximum estimated at about 4 eV.

The COM collision energy is given by:

$$E_{COM} = \frac{m}{M+m}E_k + \frac{3}{2}\frac{M}{M+m}k_B T_{cel} \tag{1}$$

where T_{cel} is the temperature of the collision cell at about 295 K. M is the mass of the cluster, m is the mass of the collision gas (H_2O or Xe) and E_k is the kinetic energy in the laboratory frame. The collision energy distribution is the result of the convolution of the

distribution of relative collision energies between the mass-selected clusters and the gas with the distribution of kinetic energies for the clusters. The COM collision energies range from about 0.073 to 0.39 eV for the H_2O attachment experiment.

The collision with the gas in the collision cell could induce ion losses due to deflections. In a recent experiment, we demonstrated such an effect for the pyrene dimer colliding with argon.[30] However, in the same study, when the pyrene dimer collided with neon, no such effects were evidenced. In the present study, larger clusters collide with water, which has about the same mass as neon. Therefore, we do not expect ion losses due to collisions, such losses being more likely the larger the ratio of cluster mass to gas mass. With respect to collisions with xenon, a similar conclusion can be drawn since, as will be shown later, similar cross sections are found for the n=6 pyrene cluster colliding with argon and xenon.

3 Experimental Results

3.1 Water Attachment Rates

Figure 2 gives the example of the mass spectrum recorded for an experiment in which a mass-selected pyrene cluster with n=9 interacted with water (vapor pressure of 8×10^{-5} mbar in the collision cell) at a kinetic energy of 5 eV in the laboratory frame. Two groups of peaks can be observed in this figure. The first group, around 151 μs corresponds to the mass-selected bare parent clusters $(C_{16}H_{10})_9^+$. The different subpeaks include isotopologues and slightly dehydrogenated species (-1H, -2H). Around 151.75 μs, new peaks appear that are due to the attachment of a single water molecule onto the bare parent cluster.

To extract cluster relative abundances, the recorded mass spectra are fitted with a multi-component fit using Gaussian functions (see Figure 2). For the water attachment analysis presented here, we used only the main subpeak corresponding to the pure ^{12}C isotopic species (subsequently referred to as the main parent species). We expect similar attachment rates for pure ^{12}C species and ^{13}C isotopologues as the difference in collision energy associated

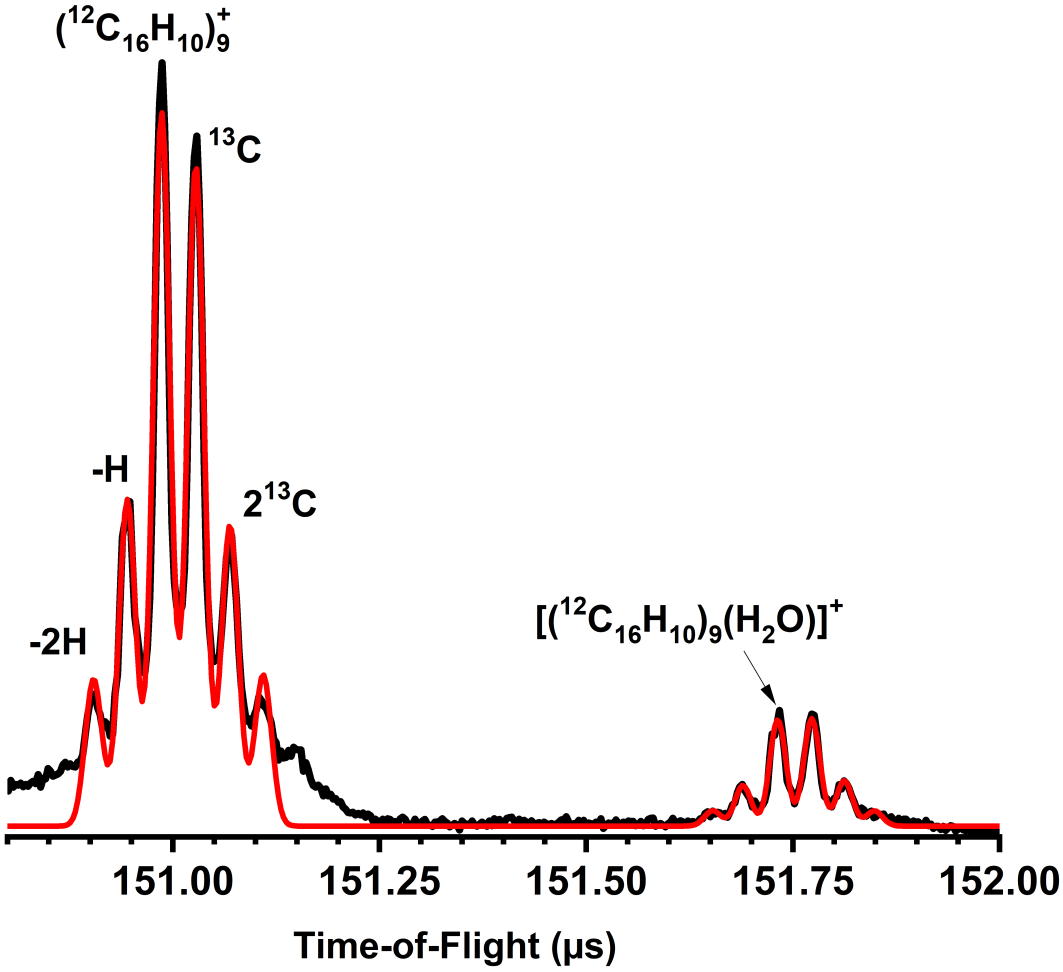

Figure 2: Time-of-flight mass spectrum of mass-selected pyrene clusters (n=9) at a kinetic energy of 5 eV in the laboratory frame. The isotopic and fragment peaks associated with the main peak (pure ^{12}C isotopomer) are residuals of the mass selection.
Peaks around 151.75 μs correspond to the attachment of one water molecule. Experimental data (black line) and multi-component fit used to extract peak intensities (red line).

with their mass difference is too small to have a noticeable effect in our experiment. The dehydrogenated species could exhibit greater reactivity, which could affect the efficiency of water molecule attachment. However, in our experimental precision, we could not see any significant difference between the attachment onto normal or dehydrogenated species. In the following, we focus on the main parent and its associated complex with H_2O.

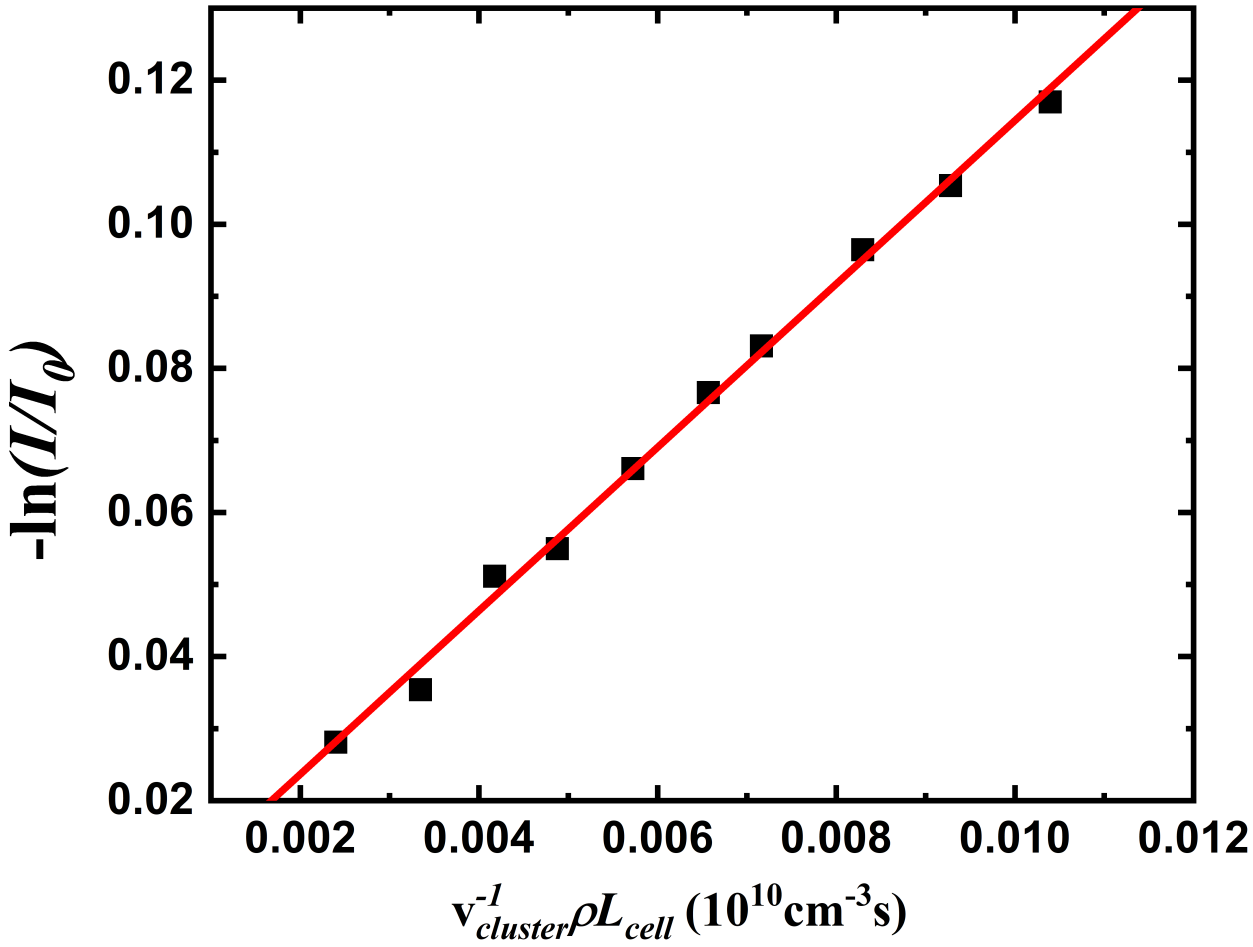

Figure 3: Evolution of $-\ln(\frac{I}{I_0})$ as a function of $\frac{\rho L_{cell}}{v_{cluster}}$ for water attachment onto mass-selected pyrene clusters of size n=9 and kinetic energy E_k=5 eV in the laboratory frame. Black squares represent experimental data points. The slope of the linear fit of the data (red line) directly gives the attachment rate, which here is (11±3) × 10^{-10} cm^3 s^{-1}.

The intensity of the parent I main peak at the exit of the collision cell can be expressed

as:

$$I = I_0 \mathrm{e}^{-\rho K_{att}^{exp} t} \tag{2}$$

where I_0 is the peak intensity at the entrance to the collision cell, K_{att}^{exp} is the experimental attachment rate, ρ is the water vapor density in the collision cell, and t is the time spent in the collision cell. The time t is deduced from the length of the collision cell L_{cell} and the speed of the cluster $v_{cluster}$ as $t = L_{cell}/v_{cluster}$. The attachment rate can then be derived from:

$$K_{att}^{exp} = -\frac{v_{cluster}}{\rho L_{cell}} \ln(\frac{I}{I_0}) \tag{3}$$

in which the intensities I and I_0 are the integrated intensity of the parent main peak and the sum of the integrated intensities of the parent and attachment peaks, respectively.

We extracted the ratio I/I_0 for each value of water vapor pressure and plotted $-\ln(\frac{I}{I_0})$ as a function of $\frac{\rho L_{cell}}{v_{cluster}}$ (see the example in Figure 3). The attachment rate is directly given by the slope of the linear fit of the experimental data. The procedure has several advantages. First, since we rely only on the variation with pressure, we do not have to worry about offsets in pressure measurements. Second, the linearity of the curve allows us to verify that no second order processes, such as multiple collisions, are involved (linear curves similar to that in Figure 3 are obtained for all cluster sizes). Third, since the experiment is repeated for each pressure, independent measurements of the cross-section are made and a better statistic is obtained.

In determining the attachment rate, the following sources of systematic uncertainty must be considered. First, as mentioned earlier, we do not expect the effective cell length to differ substantially from its physical length. However, to be conservative, we take an uncertainty of 10%. For the cluster velocity, based on the simulated trajectories, we estimate the uncertainty to be less than 5%. The main uncertainty probably comes from the pressure measurement,

although the gas correction factors obtained from the comparison of the ionization gauge and the capacitive gauge used are similar to those found in the manufacturers' manuals. Finally, we estimate that the combined uncertainty from the gas density, cluster velocity and cell length to be about 25%. For the example given in Figure 3, taking into account this systematic uncertainty leads to $K_{att}^{exp} = (11 \pm 3) \times 10^{-10}$ cm^3 s^{-1}. Furthermore, from multiple experimental realizations, we extract the standard deviation error. In the following, the error bars shown in the figures represent, when available, this experimental one standard deviation.

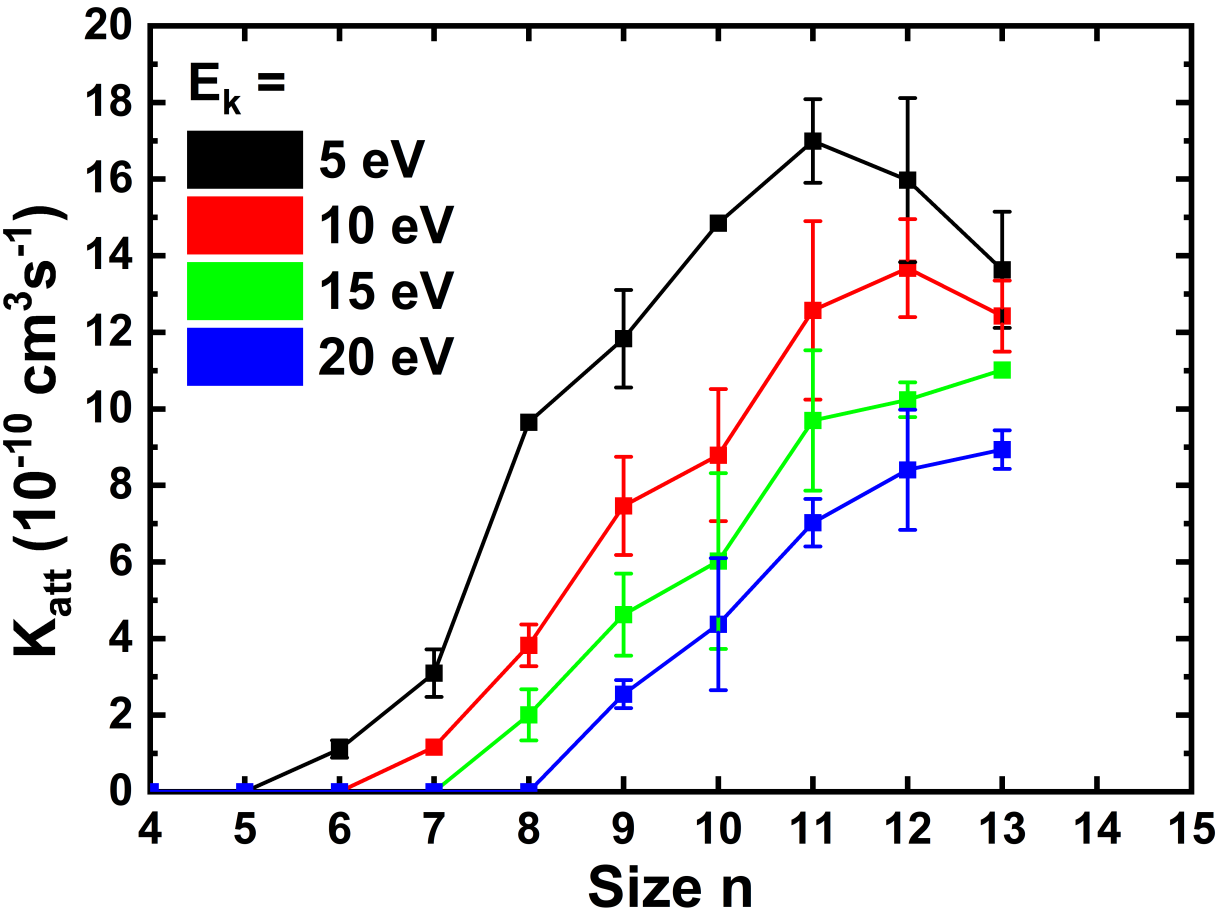

Figure 4: Water attachment rates on mass-selected pyrene clusters as a function of size for different kinetic energies in the laboratory frame.

Figure 4 compiles the derived water attachment rates as a function of cluster size for four different kinetic energies in the laboratory frame. An increase of the rates with cluster size is observed as expected for larger clusters that have larger collision cross-sections. For cross-sections that do not depend on relative velocities, such as geometric cross-sections, one would expect the attachment rate to increase with kinetic energy, this rate being proportional to the relative velocity. However, we observe for a given size a decrease in the attachment rate with increasing laboratory collision energy (or E_{COM}). In addition, there is a threshold in size for the observation of water attachment that depends on the kinetic energy. For instance, at 20 eV, we do not see attachment below n=9, whereas at 5 eV, we observe attachment for sizes down to n=6. Figure 5 shows the same data as Figure 4 but as a function of E_{COM}. Each size has a different threshold in E_{COM} for attachment to be observed. For example, for n=6, no attachment is observed for collision energies above 0.17 eV. The threshold is between [0.16-0.22 eV] for n=7, [0.20-0.25 eV] for n=8 and probably above 0.3 eV for n=9. For larger masses, the threshold value increases further but it is more difficult to derive intervals due to the lack of data at higher E_{COM}. These results imply that the attachment efficiency depends on E_{COM}. Finally, we observe in Figure 4 that the attachment rates decrease slightly for the largest sizes (above n=11) and the lowest kinetic energies in the laboratory frame (5 and 10 eV). Possible explanations for this behavior will be explored in section 4.

3.2 Sticking Coefficient

The adsorption rate of a molecule on a surface is usually given by the product of the sticking coefficient by the collision rate. In order to derive collision rates, we used the following procedure. First, we measured the dissociation rates of pyrene clusters upon collisions with Xe atoms with a high E_{COM} of 10 eV. Under these conditions, we observed a complete dissociation cascade down to the monomer ion for all sizes studied (see Figure 6 for size n=6). This is consistent with previous measurements of dissociation energies of cationic pyrene clusters,[30] from which we can deduce that complete dissociation requires about 9 eV

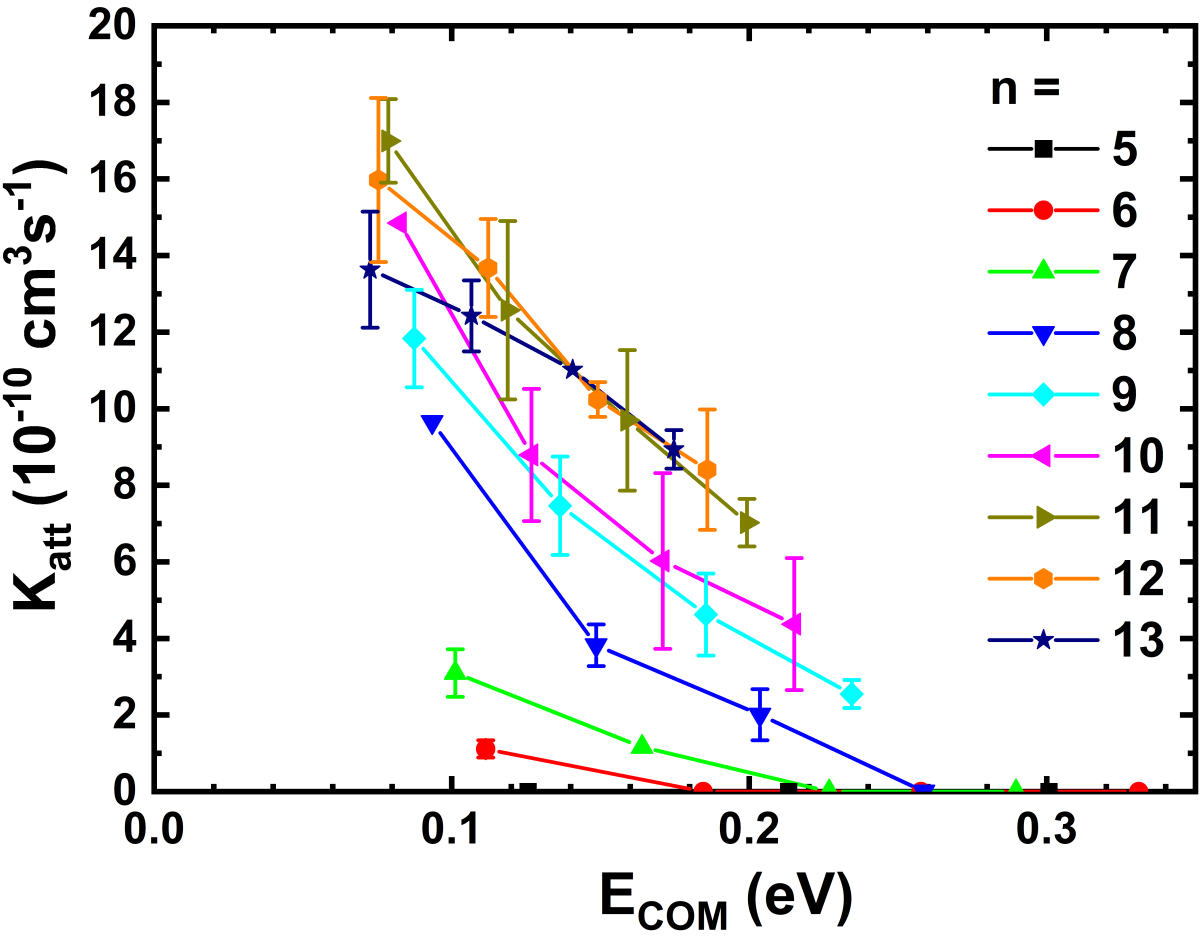

Figure 5: Water attachment rate onto mass selected pyrene clusters as a function of E_{COM}.

of total energy for the size range considered here. Dissociation rates are obtained in a very similar way to attachment rates by extracting peak intensities and using the right-hand side of Equation 3. All peak intensities (isotopic, dehydrogenated) are included in the calculation considering that the neutral fragment can come from any parent peak multiplet. Figure 7 plots $-\ln(\frac{I}{I_0})$ as a function of $\frac{\rho L_{cell}}{v_{cluster}}$ for the dissociation of mass-selected pyrene clusters with n=6 at E_{COM}=10 eV. The slope of the curve gives us directly the dissociation rate. A similar linear behavior is observed for all sizes studied. This procedure was applied to all clusters of size n=6 to 13.

In a second step, we derived the geometric cross-section of the clusters using the following theoretical expression for the dissociation rate:

$$K_{diss} = \int_0^{+\infty} dv_{rel} f(v_{rel}) v_{rel} \sigma_{diss} \tag{4}$$

with the expression of the dissociation cross-section given in Armentrout et al.:[31]

$$\sigma_{diss} = (\sigma_0 p / E_{COM}) \int_{E_0 - E_{ini}}^{E_{COM}} d\varepsilon \left(1 - \mathrm{e}^{-k_{diss}(\varepsilon + E_{ini})\tau}\right) (E - \varepsilon)^{p-1} \tag{5}$$

where σ_0 is the geometric cross-section, p is an empirical parameter for collision energy deposition, k_{diss} is the unimolecular dissociation rate, and τ is the experimental time available for dissociation. E_0 is the dissociation energy, and E_{ini} is the initial internal energy of the cluster at 25 K. We used previously estimated values for the unimolecular dissociation rate and dissociation energy for each cluster size.[30,32] The parameter p was taken equal to 1 and the geometric cross-section σ_0 was fitted to reproduce the experimental dissociation rates. Figure 8 shows the derived values for σ_0, which, as expected, increase with size. Good agreement is found with values derived in a previous study of CID of pyrene clusters for sizes n=2 to 6, although using argon as the collision gas.[30] This agreement is probably due to the fact that the difference in van der Waals radii, namely 1.88 Å for Ar and 2.16 Å for Xe,[33] is small relative to the cluster size.

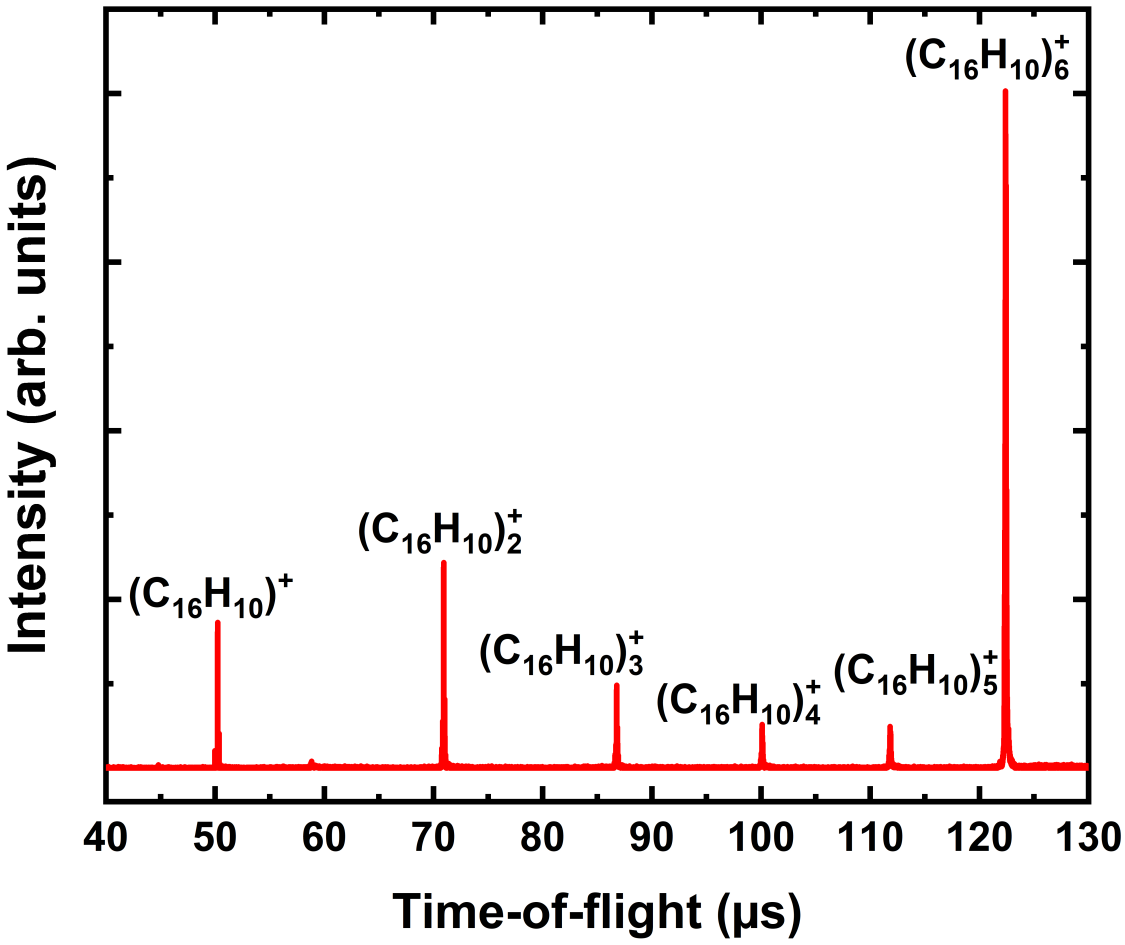

Figure 6: TOF-MS of a mass-selected pyrene cluster (n=6) colliding with xenon at E_{COM}=10 eV. The pressure of xenon in the collision cell is 2 $\times$ 10^{-4} mbar, leading to an average number of collisions of 0.41.

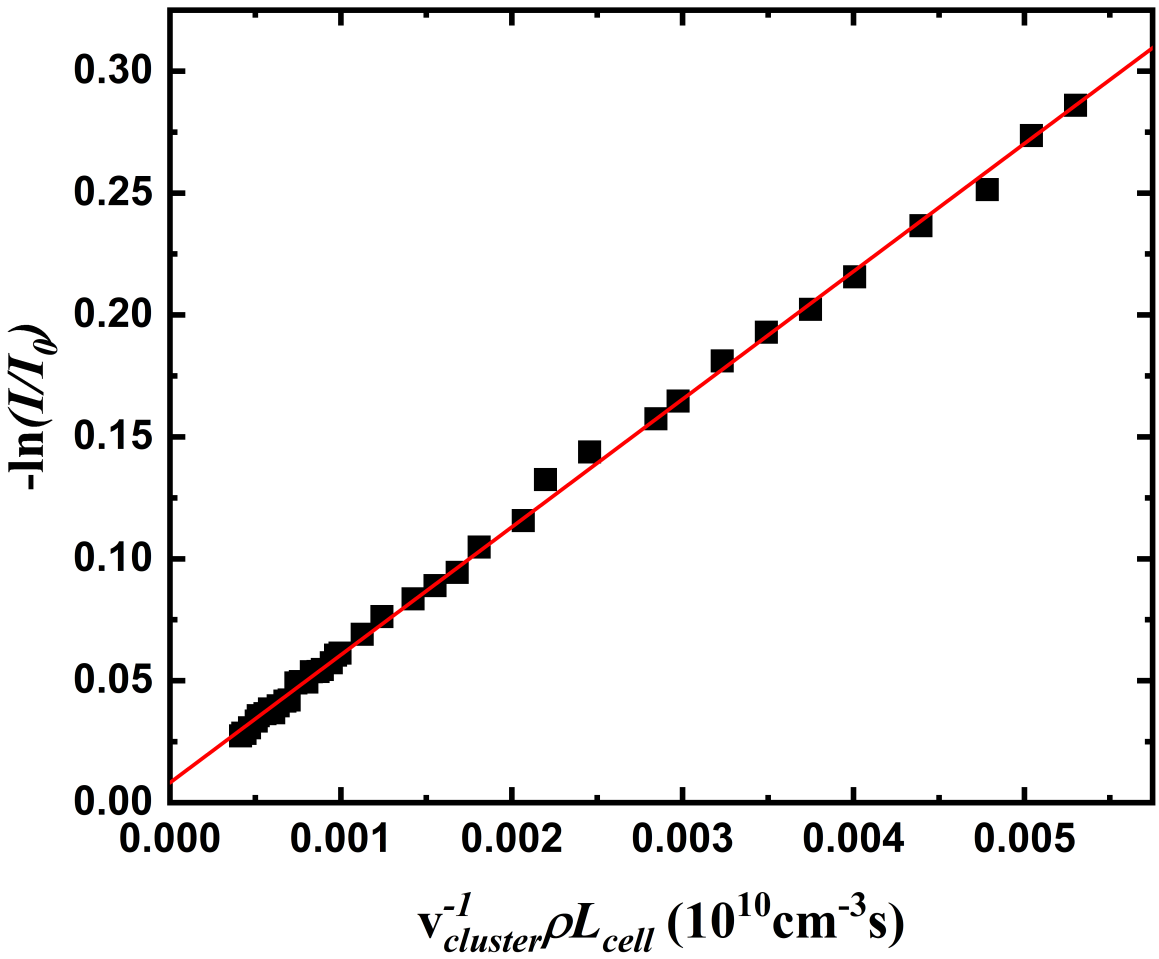

Figure 7: Evolution of $-\ln(\frac{I}{I_0})$ as a function of $\frac{\rho L_{cell}}{v_{cluster}}$ for dissociation of mass-selected pyrene clusters of size n=6 and E_{COM}=10 eV. Black squares represent experimental data points. The slope of the linear fit of the data (red line) directly gives the dissociation rate, which here is (52±13) $\times$ 10^{-10} cm^3 s^{-1}.

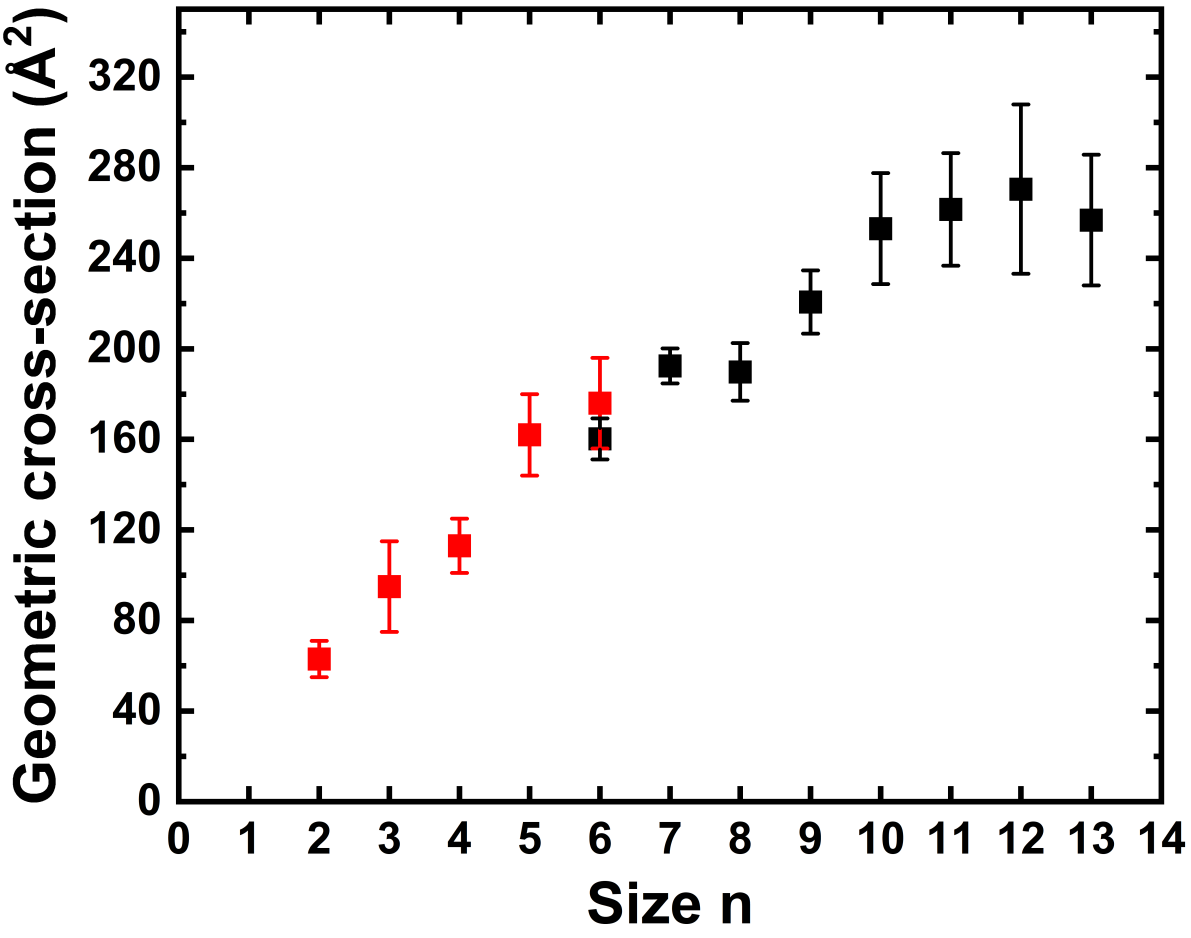

Figure 8: Geometric cross-section as a function of pyrene cluster size. Black squares: current study. Red squares: results from previous CID experiments.[30]

Finally, we derive the geometric collision rate $K_{geo} = \sigma_0 \overline{v_{rel}}$ (see Supporting Information), and calculate the sticking coefficient by dividing the measured attachment rate by the geometric collision rate. We present the variation of the sticking coefficient as a function of cluster size and COM collision energies in Figure 9 and Figure 10, respectively. A maximum sticking coefficient of 0.6-0.7 is obtained at the lowest collision energy and for the largest clusters ($n \geq 8$).

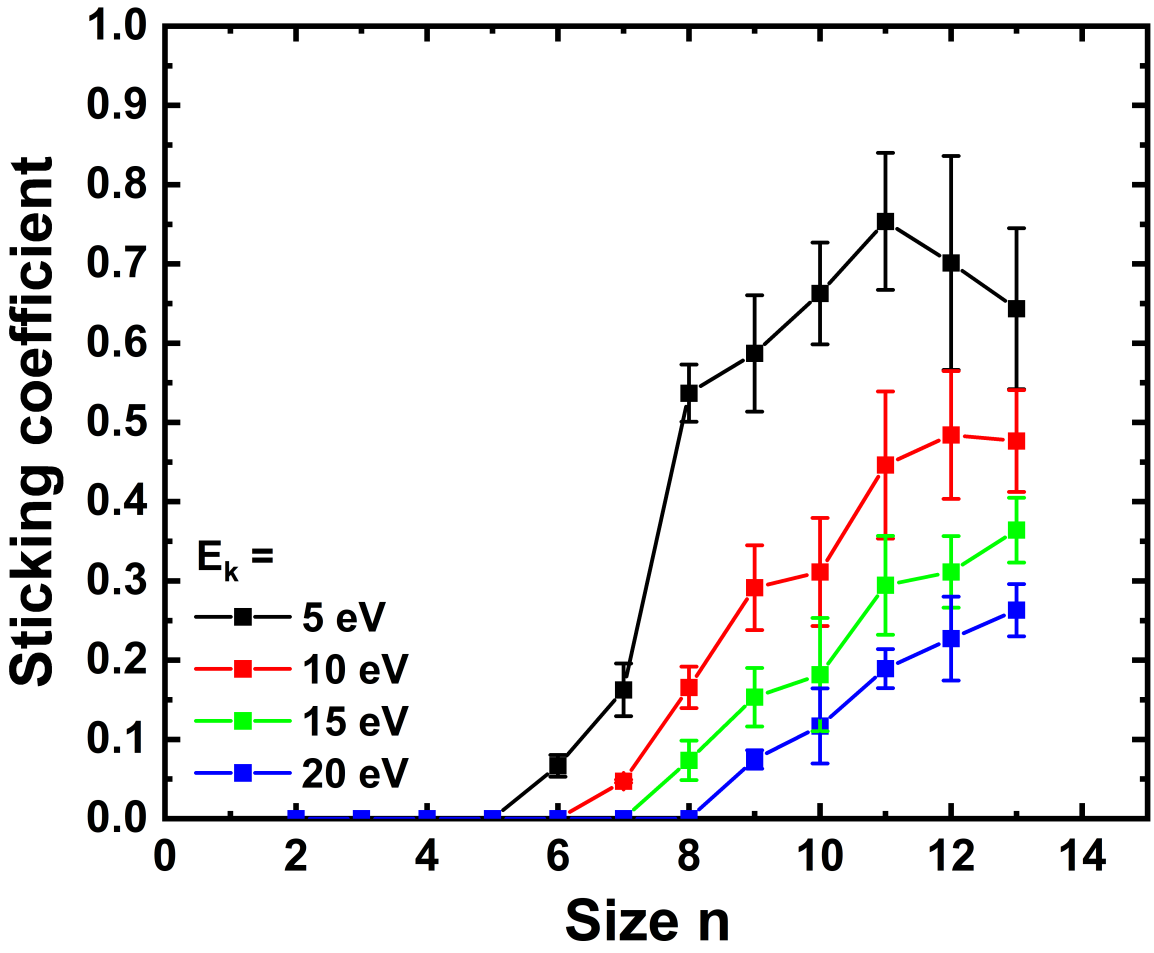

Figure 9: Sticking coefficient of water on mass-selected pyrene clusters as a function of cluster size.

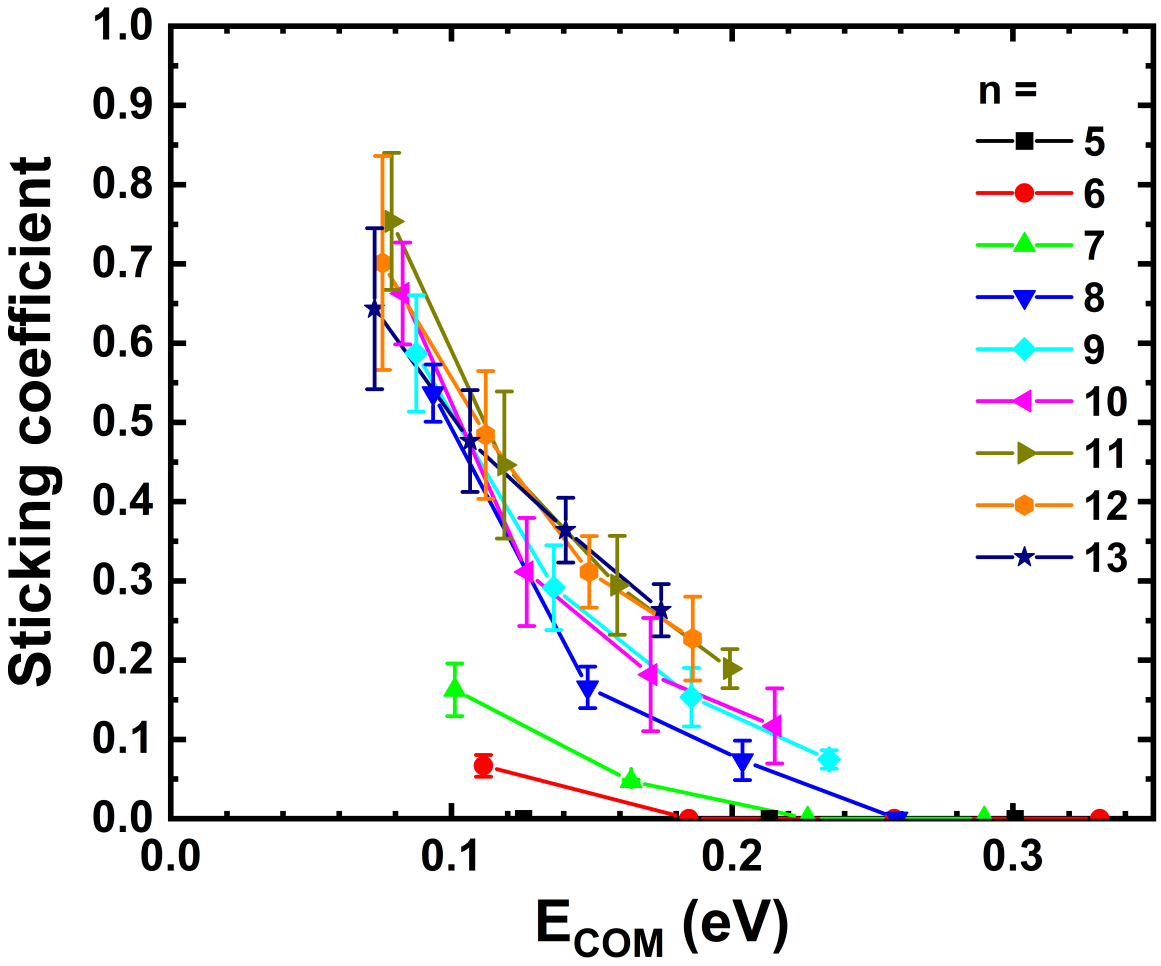

Figure 10: Sticking coefficient of water on mass-selected pyrene clusters as a function of E_{COM}.

4 Discussion

The attachment rate of a water molecule to mass-selected pyrene cluster cations was measured for four different kinetic energies in the laboratory frame. No attachment or very inefficient attachment is observed for the smallest clusters studied (n≤6). For the other clusters, it is observed that the attachment rate increases with the cluster size. This trend is observed for all E_{COM} energies with a decrease of the rate when E_{COM} increases. In the following, we discuss how these results can be rationalized using a theoretical description of the attachment rate. We show that such a model can only account for the experimental results obtained for the largest clusters. For the others, the observed rate is significantly smaller than the calculated rate, indicating a competing process. The latter is attributed to statistical dissociation for an internal energy of the cluster that corresponds to the sum of E_{COM} and the water-cluster binding energy. A good agreement of the model with the experimental results can be obtained by taking into account the dissociation. The extension to relevant astrophysical conditions is then discussed.

4.1 Model for the Collision Rate

Depending on the type of interaction between the colliding partners, the collision cross-section, and thus the collision rates, are expected to depend on the velocity. If we assume, for example, a geometric collision cross-section and that each collision leads to attachment, then the attachment rate, for a given size, should increase as the relative velocity increases (see Supporting Information). This is clearly not the case in our experiment since we observe that the attachment rate decreases with increasing kinetic energy in the laboratory frame.

In the case of a polar molecule with a permanent dipole interacting with an ion, we can derive the collision rates from the Langevin cross-section. We give in the Supporting Information the expression for the Langevin[34,35] rate in the average dipole orientation (ADO) approximation,[36–39] which we will refer to below as ADO rates. Figure 11 shows both the

calculated ADO rates and the experimental water attachment rates. The values of the dipole locking constants given in Table 1 provide a good match between the ADO rates and the measured rates for the largest sizes. These values are consistent with the ADO approximation: as the relative velocity decreases, the dipole moment of the water molecule has more time to align in the ion field, and the dipole lock constant is larger.

Table 1: Dipole locking constant values that allows to best reproduce the experimental results.

E_k (eV)	5	10	15	20
C	0.35	0.30	0.25	0.17

Figure 11 shows that the ADO rates are only able to account for the experimental rates overall for the largest sizes. The observed decrease in rates for n=12-13 at the lowest kinetic energies (5 and 10 eV) is not present in the ADO rates. Furthermore, the decrease in experimental rates with cluster size is not correctly explained by the ADO rates.

A number of limitations of the calculated ADO rates are listed below. First, in the current approach, we did not take into account the finite size of the clusters. As the size increases, at some point the geometric cross-section will become larger than the Langevin cross-section. Some corrections have been proposed to account for this finite size effect.[40] However, in our case, we observe that even for the largest size, the measured attachment rate and the predicted Langevin rate are smaller than the geometric rate. On the other hand, neither the geometric rates nor the ADO rates predict the decay of the attachment rate for the largest sizes at the two lowest kinetic energies (5 and 10 eV). This behavior could be due to a greater dilution of charge within the largest clusters, resulting in a decrease in the magnitude of the ion-induced dipole interaction or ion-dipole interaction. However, it has been shown that the charge tends to remain mainly localized on two to three central units of pyrene clusters.[41] In this case, the charge would be partially shielded with increasing size, leading to a decrease in attractive forces, which may explain the observed feature in the experimental attachment rate onto the largest clusters.

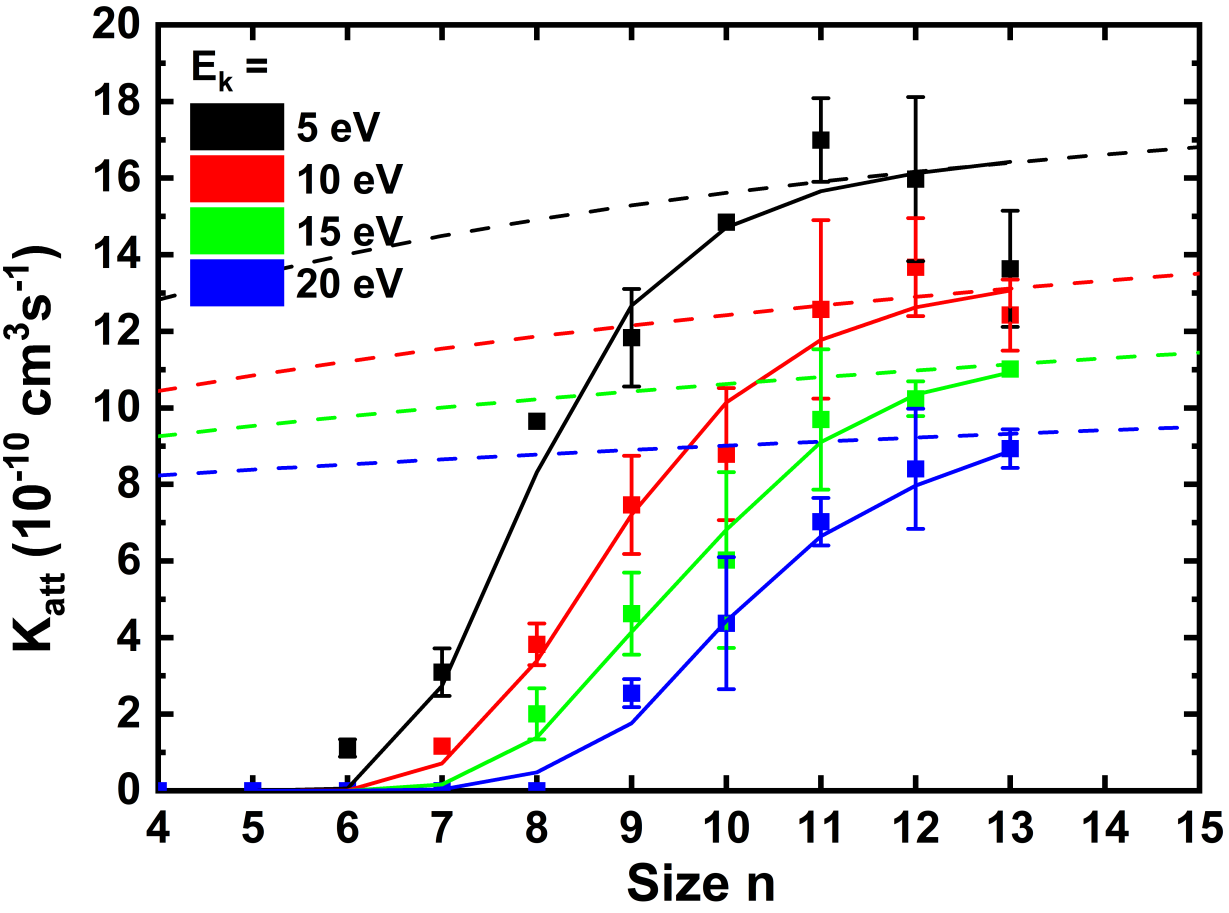

Figure 11: Water attachment rates onto mass-selected pyrene cluster cations as a function of cluster size. Experimental results are shown as squares . ADO rates using the C values given in Table 1 are represented by dashed lines. The solid lines are the results of a model that includes dissociation. This model is described later in the text. The colors correspond to the different studied kinetic energies in the laboratory frame.

Despite these limitations, we consider the calculated ADO collision rates to account for both the effective attractive potential between the ion and the water molecule and the average over the complex details of the collision, such as the dependence of the H_2O landing site attachment onto the cluster or the relative orientation of the molecule with the cluster.

4.2 Model with Statistical Dissociation

As we pointed out in the previous section, the observed attachment rates cannot be explained by simply considering Langevin-type capture cross-sections. As we will show in this section, the experimental results can be explained by taking into account statistical dissociation after water attachment.

Given the initial internal energy of the cluster E_{ini}, the internal energy of the water-pyrene cluster cation formed upon attachment is given by:

$$E_{int} = E_{ini} + E_{COM} + D_n \tag{6}$$

where D_n is the dissociation energy of the water molecule from the cluster of size n. The average collision energy depends on the dependence of the cross-section on the relative velocity. However, as can be seen in the Supporting Information, taking this effect into account results in only minor corrections. For a given collision energy, the redistribution, between degrees of freedom, of collision and dissociation energies should primarily dictate the fate of water attachment.

The internal energy after collision can be converted into a temperature by making use of previous works in which the vibrational modes of pyrene clusters of various sizes were obtained based on DFTB calculations.[32,42] The average internal energy of the pyrene clusters as a function of temperature is calculated using the vibrational modes with:

$$E_{th}(T) = \sum_i \frac{\hbar\omega_i}{e^{\hbar\omega_i/k_BT} - 1} \tag{7}$$

where the sum over i is for all harmonic vibrational modes of the pyrene cluster. We neglect here the intermolecular modes between the water molecule and the pyrene cluster. We then derive the temperature T of the cluster after water molecule attachment by numerically solving:

$$E_{th}(T) = E_{th}(25K) + D + E_{COM} \tag{8}$$

The binding energy for the water-naphthalene cation was measured to be approximately 0.33 eV.[43,44] The binding energies were calculated for the same species at the DFT level and range from 0.2 to 0.4 eV depending on the binding site and the DFT functional used.[44,45] For the water-coronene cation, calculations at the DFT level gives very similar binding energies, namely 0.25 and 0.39 eV depending on the binding site.[46] In the following, we will use a value of D =0.3 eV for the binding energy of water on the cationic pyrene clusters. A different value will affect the derived temperature for the clusters

After the attachment of a water molecule, the cluster may be too hot to survive long enough to be detected. We describe in the Supporting Information a model that satisfactorily reproduces the experimental results. In this model, the attachment rate is described using the ADO rate, as discussed in the previous section. After attachment, we extract the cluster temperature as described above and use it to quantify the unimolecular dissociation rate using the simple following expression:

$$k_{diss} = Ae^{-D/kBT} \tag{9}$$

Here D is the water-pyrene cluster binding energy, and A is a prefactor. Using a value of $D = 0.3$ eV, as discussed earlier, we fitted the prefactor to A =(10±5) $\times$ 10^{16} s^{-1} so that the dependence of the attachment rates with E_{COM} and the cluster size is reproduced. The good agreement between the model and the experimental results (see Figure 11) confirms the role of statistical dissociation in the measured attachment rates. The upper and lower limits we give for the prefactor value are obtained from the fit goodness being degraded by 25%. We

note that the value of the prefactor is quite sensitive to the choice of the dissociation energy. Indeed, when the latter quantity is varied by ± 0.02 eV, the optimal value obtained for A goes from about 3×10^{16} s^{-1} to 30×10^{16} s^{-1}, with negligible degradation of the fit goodness.

The expression for the dissociation rate used here is rather crude. A rigorous description of dissociation would first require taking into account the angular momentum transferred to the complex upon attachment. This implies taking into account the distribution of the impact parameters as well as the relative velocity distributions. Then, the dissociation of the energized complex formed would ideally be treated with the statistical theories PST or RRKM. In order to be compared with experiments, these rates should then be averaged over a number of distributions, such as internal energies, angular momentum and relative velocities. Such a treatment has already been used successfully by Koizumi and Armentrout.[47] However, in our case, a description of the ground-state electronic structure of the molecular complexes studied would be required to determine which isomers can be populated upon attachment. Such a study was performed, for example, in the case of pyrene clusters at a given temperature in Ref.[48]. This is a necessary step in determining the vibrational frequencies to be used in the PST or RRKM statistical theories. Overall, a more sophisticated model of the dissociation rate would require a significant amount of work that is beyond the scope of this article.

4.3 Comparison with Surface Experiments

The attachment rate as a function of cluster temperature is plotted in Figure 12. Examination of this figure shows that there is a threshold for the observation of attachment at about 140 K.

As the temperature rises, statistical dissociation limits the observation of attachment, leading to the apparition of a threshold. At low temperature, where the statistical dissociation becomes less important, larger variations are observed due to the size dependence of the attachment rates.

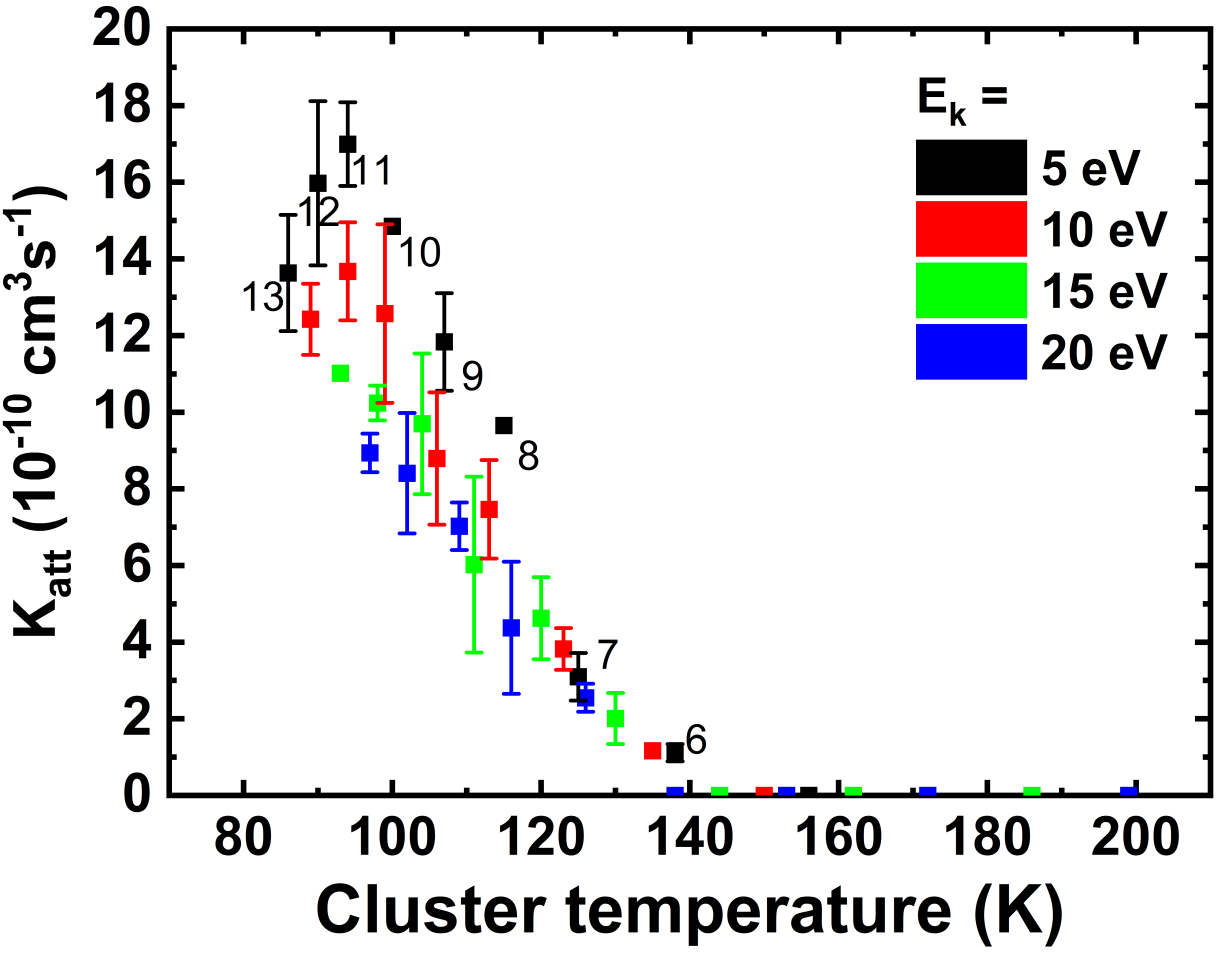

Figure 12: Water attachment rates onto mass-selected pyrene clusters as a function of cluster temperature after collision. The given numbers correspond to the black points and indicate the corresponding cluster size for the attachment rate at 5 eV.

Interestingly, the decrease of the attachment rate with temperature as observed in Figure 12 appears in line with the onset of water desorption observed at 130-140 K in temperature-programmed desorption (TPD) experiments for H_2O ices deposited on graphite surfaces or carbon nanotubes.[49,50] TPD is a rather complicated process involving molecules migrating on the surface, multilayer interaction, etc. In this respect, the reverse attachment process observed here on isolated clusters seems simpler to quantify gas-grain interactions.

In the present study we use a value of 0.3 eV for the dissociation energy because, as mentioned earlier, it appears to be a typical value for the binding energy of water to similar systems. Desorption energies of about 0.4-0.5 eV are deduced from TPD experiments, which are comparable (but a bit higher) to the dissociation energy used in this study. Using a value of D=0.5 eV in our model (which is likely an extreme value) would lead to a less well defined threshold at about 170 K. We give in the Supporting Information the dependence with temperature of the attachment rate for dissociation energies from 0.1 to 0.5 eV.

4.4 Astrophysical Implications

The present experimental work can be used to gain insights into water-nanograin interactions in an astrophysical context, with pyrene clusters serving as models for these nanograins. The main difference between the experimental conditions and the conditions that prevail in astrophysical environments concerns time scales. The microsecond limit in our TOF-MS experiment does not apply to conditions in space, where the limit is given by the slowest processes, specifically radiative cooling by infrared (IR) emission. In previous work, IR cooling rates for PAH clusters were estimated by multiplying the IR rate of the isolated PAH by the number of units in the cluster.[10,11] The k_{IR} values for $C_{16}H_{10}^+$ were calculated using a Monte Carlo code developed to simulate the photophysics of PAHs.[51,52] We used the scaled harmonic vibrational frequencies and IR intensities available in the theoretical spectral database of polycyclic aromatic hydrocarbons[53] and calculated the density of states using a modified version of the Beyer-Swinehart algorithm[54] that provides a smooth density

down to low energies.[52] Calculated k_{IR} values for $C_{16}H_{10}^{+}$ are 0.7 and 2.0 s^{-1} at 0.3 and 0.5 eV, respectively. In the case of the clusters, a comparable amount of internal energy is involved but distributed over the whole clusters. For these low energies the contribution of low frequency intermolecular modes[55] cannot be neglected. However, this contribution cannot be quantified since the complete vibrational spectrum of the pyrene cluster cations has only been calculated for sizes up to n=4.[42] In the following, we therefore consider the value of k_{IR} per pyrene unit to be between 0.1 and 1.0 s^{-1}.

The competition between the unimolecular statistical dissociation of the water molecule and the cooling by IR emission allows us to define a size dependent critical temperature T_C below which the complex will survive. This can be expressed as follows:

$$k_{diss}(T_c) = n \times k_{IR} \tag{10}$$

with k_{diss} deduced from the present study (Equation 9) and k_{IR} estimated above. This leads to:

$$T_c = \frac{D}{k_B \ln\left(\frac{A}{nk_{IR}}\right)} \tag{11}$$

In a gas at kinetic temperature T_{gas}, the internal energy of the complex formed by the attachment of a water molecule onto a PAH cluster of size n and initial temperature T_{ini}, is given by:

$$E(T) = E(T_{ini}) + D + 2k_B T_{gas} \tag{12}$$

where D is the binding energy of the water onto the cluster and $2k_B T_{gas}$ is the average collision energy.

The critical temperature T_c can be used to deduce the maximum gas temperature below which the formation of a long lived water-cluster complex is possible:

$$T_{gas} = \frac{E(T_c) - D - E_{ini}(T)}{2k_B} \tag{13}$$

We present in Figure 13 the derived values of T_{gas} as a function of cluster size for k_{IR} =0.1 and 1.0 s^{-1}, and two different initial temperatures of the cluster, namely 0 and 50 K. Figure 13 shows a very strong increase of the maximum gas temperature with the cluster size. Considering the case with T_{ini}=50 K and k_{IR} =1.0 s^{-1}, the minimum size required for complex survival increases from n=11 to n=14 for T_{gas} between ∼10 K in cold clouds[56] and ∼500 K in hot molecular gas associated with star-forming regions.[57] This shows that the survival of the water-cluster complex during formation does not depend much on T_{gas}. Rather, it depends on the temperature of the complex, as expected from thermal evaporation or more generally thermal desorption from grains.[58] One of the key issues in gas-grain interactions is the efficiency of desorption of molecules from grain surfaces. In a number of environments, thermal desorption is not efficient because the grains do not reach high enough temperatures. This will not be the case for PAH clusters that can reach significant temperatures upon photoexcitation or collision with cosmic rays. A temperature of at least 140 K that would lead to efficient desorption can be reached with an energy of 0.07 eV per pyrene molecule (Figure S1), which would imply an energy of 1 eV for a pyrene cluster with n=14. Near-IR photons can penetrate much deeper in molecular clouds than UV photons, with an optical depth that is typically 20 times smaller.[59] These photons can be absorbed very efficiently by cationic clusters, which exhibit very strong charge transfer transitions in this range.[60] Neutral (and cationic) clusters would absorb efficiently at energies above ∼4 eV, as expected from the photoabsorption spectrum of the pyrene molecule.[61]

5 Conclusion

We reported the measurement of water molecule attachment rates onto cationic pyrene clusters of selected size. These rates were measured as a function of cluster size and collision energy in the laboratory frame. From the comparison of the attachment rate with CID experiments we were able to derive values for the sticking coefficient. The dependence of the

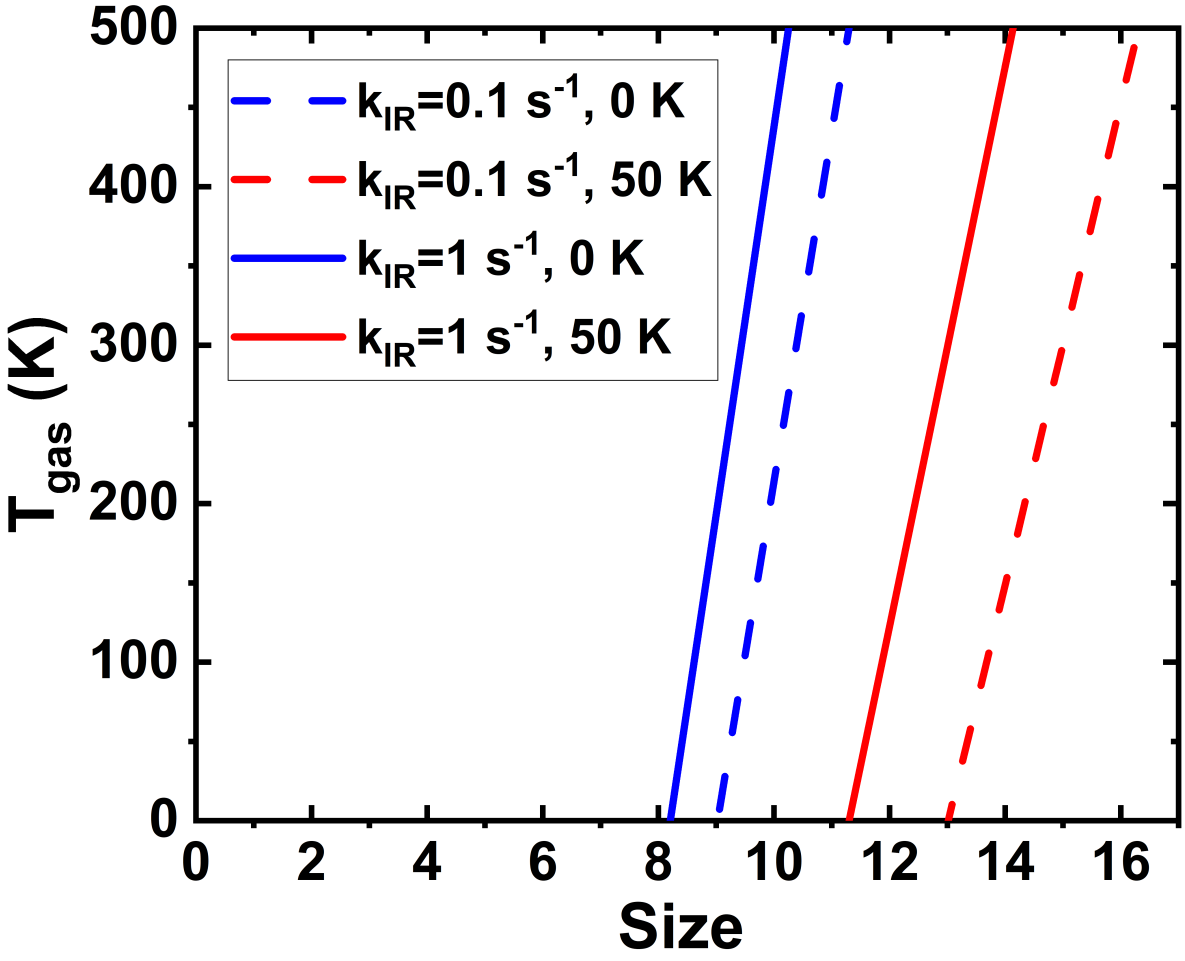

Figure 13: Estimation of the survival of the water-pyrene cluster complex following its formation under astrophysical conditions as a function of the gas temperature and the cluster size. Two different initial cluster temperatures (0 and 50 K) are considered as well as two values of k_{IR} per pyrene unit, 0.1 and 1.0 s^{-1}.

attachment rate on size and kinetic energy was then rationalized using a model in which we use a Langevin-type collision rate in the ADO approximation. We show that the attachment is limited by the lifetime of the formed water-PAH cluster complex. Upon attachment of a water molecule, the internal energy is increased by a significant amount, namely the dissociation energy plus the collision energy (E_{COM}). This increase in energy can lead to statistical dissociation on the time scale of the experiment. By including statistical dissociation in the model, we were then able to rationalize experimental results. The attachment rates were also plotted as a function of temperature of the water-pyrene cluster complex. The data show a threshold at about 140 K above which the observation of attachment is excluded in our experiment. A similar temperature threshold value is observed in TPD experiments on carbon surfaces. Fitting the experimental data with the model allowed us to quantify the dissociation rate and derive an estimation of the survival of the water-pyrene complex under astrophysical conditions.

In the analysis of our results, we only considered statistical dissociation after attachment. However, dynamical effects could also play a role. For example, if the collision is too fast, we can consider the collision to be purely impulsive.

Such a dynamical effect, which would depend on the details of the collision itself, would require extensive molecular dynamics simulations to be properly described. Such effects have for example been studied for the attachment of water molecules onto nano-aerosols[62] or onto protonated water clusters.[63] Another limitation to the application of the results to the astrophysical context is the quantification of the radiative cooling rate involved in stabilizing the water-cluster complex. We also note that the effects of angular momentum have not been taken into account here.

This experimental work is a first step in the study of the interaction of the H_2O molecule with PAH clusters which are considered to be analogues of interstellar eVSGs. While recent experiments have considered the finite size of interstellar dust, none have been performed for nanograins that are in the gas phase and not supported by a substrate. The clusters we

have studied here are (sub-)nanometric in size. For the larger ones, a typical radius of 7 Å can be deduced from the geometrical cross section. Because of this small size, these clusters undergo a temperature change upon collision with a water molecule that could be sufficient to cause subsequent evaporation of the adsorbed molecule. We determined that cluster sizes of at least nine pyrene molecules are needed for the attachment to persist in astrophysical long time scales.

In the present study, the observation of attachment was limited by the lowest attainable collision energy. Another way to study the properties of these water-PAH complexes would be to produce such species in the gas aggregation source. The stability of these clusters can then be studied either by varying their initial temperature or by threshold CID. Such studies have already been undertaken for pyrene cluster cations[30,32] and can be easily performed on these mixed water-pyrene clusters.

A recent study concluded on the interest of modeling the physical and chemical evolution of PAH clusters in protoplanetary disks.[64] The kinetic measurements reported in our article as well as our previous work on the stability of bare PAH clusters[30,32] can be used in models of protoplanetary disks (e.g. Kamp et al.[65]) among other astrophysical environments. The link to observations will be greatly enhanced in the very near future by the unprecedented spectroscopic and angular resolution capabilities of the James Webb Space Telescope. This infrared space telescope will open up the possibility of studying the relationship between aromatic and aliphatic hydrocarbon matter[66,67] and ices.[68] It will provide us with new information on gas-dust interactions to test different ice-grain scenarios.

Supporting Information Available

In the Supporting Information, we derive the expressions for the geometric and ADO collision rates and the average collision energy for the ADO cross section. We also present the model used to reproduce the data.

Acknowledgement

This work received support from the European Research Council under the European Union's Seventh Framework Programme ERC-2013-SyG, Grant Agreement no. 610256, NANOCOS-MOS. This project has received financial support from the CNRS through the 80|Prime program (Project Nano-eau).

References

(1) Dobbins, R.; Fletcher, R.; Chang, H.-C. The evolution of soot precursor particles in a diffusion flame. *Combustion and Flame* **1998**, *115*, 285–298.

(2) Jacobson, R. S.; Korte, A. R.; Vertes, A.; Miller, J. H. The Molecular Composition of Soot. *Angewandte Chemie International Edition* **2020**, *59*, 4484–4490.

(3) Sabbah, H.; Biennier, L.; Klippenstein, S. J.; Sims, I. R.; Rowe, B. R. Exploring the Role of PAHs in the Formation of Soot: Pyrene Dimerization. *J. Phys. Chem. Lett.* **2010**, *1*, 2962–2967.

(4) Mercier, X.; Carrivain, O.; Irimiea, C.; Faccinetto, A.; Therssen, E. Dimers of polycyclic aromatic hydrocarbons: the missing pieces in the soot formation process. *Phys. Chem. Chem. Phys.* **2019**, *21*, 8282–8294.

(5) Allamandola, L. J.; Tielens, A. G. G. M.; Barker, J. R. Interstellar Polycyclic Aromatic Hydrocarbons: The Infrared Emission Bands, the Excitation/Emission Mechanism, and the Astrophysical Implications. *Astrophys. J., Suppl. Ser.* **1989**, *71*, 733.

(6) Peeters, E.; Spoon, H. W. W.; Tielens, A. G. G. M. Polycyclic Aromatic Hydrocarbons as a Tracer of Star Formation? *Astrophys. J.* **2004**, *613*, 986–1003.

(7) Rapacioli, M.; Joblin, C.; Boissel, P. Spectroscopy of polycyclic aromatic hydrocarbons and very small grains in photodissociation regions. *Astron. Astrophys.* **2005**, *429*, 193–204.

(8) Berné, O.; Joblin, C.; Deville, Y.; Smith, J. D.; Rapacioli, M.; Bernard, J. P.; Thomas, J.; Reach, W.; Abergel, A. Analysis of the emission of very small dust particles from Spitzer spectro-imagery data using blind signal separation methods. *Astron. Astrophys.* **2007**, *469*, 575–586.

(9) Pilleri, P.; Montillaud, J.; Berné, O.; Joblin, C. Evaporating very small grains as tracers of the UV radiation field in photo-dissociation regions. *Astron. Astrophys.* **2012**, *542*, A69.

(10) Rapacioli, M.; Calvo, F.; Joblin, C.; Parneix, P.; Toublanc, D.; Spiegelman, F. Formation and destruction of polycyclic aromatic hydrocarbon clusters in the interstellar medium. *Astron. Astrophys.* **2006**, *460*, 519–531.

(11) Montillaud, J.; Joblin, C. Absolute evaporation rates of non-rotating neutral polycyclic aromatic hydrocarbon clusters. *Astron. Astrophys.* **2014**, *567*, A45.

(12) Henning, T.; Semenov, D. Chemistry in Protoplanetary Disks. *Chemical Reviews* **2013**, *113*, 9016–9042, PMID: 24191756.

(13) Piso, A.-M. A.; Öberg, K. I.; Birnstiel, T.; Murray-Clay, R. A. C/O and Snowline Locations in Protoplanetary Disks: The Effect of Radial Drift and Viscous Gas Accretion. *Astrophys. J.* **2015**, *815*, 109.

(14) Drążkowska, J.; Alibert, Y. Planetesimal formation starts at the snow line. *Astron. Astrophys.* **2017**, *608*, A92.

(15) Öberg, K. I.; Bergin, E. A. Astrochemistry and compositions of planetary systems. *Physics Reports* **2021**, *893*, 1–48, Astrochemistry and compositions of planetary systems.

(16) Pauly, T.; Garrod, R. T. The Effects of Grain Size and Temperature Distributions on the Formation of Interstellar Ice Mantles. *Astrophys. J.* **2016**, *817*, 146.

(17) Iqbal, W.; Wakelam, V. Nautilus multi-grain model: Importance of cosmic-ray-induced desorption in determining the chemical abundances in the ISM. *Astron. Astrophys.* **2018**, *615*, A20.

(18) Sipilä, O.; Zhao, B.; Caselli, P. Effect of grain size distribution and size-dependent grain heating on molecular abundances in starless and pre-stellar cores. *Astron. Astrophys.* **2020**, *640*, A94.

(19) Gavino, S.; Dutrey, A.; Wakelam, V.; Guilloteau, S.; Kobus, J.; Wolf, S.; Iqbal, W.; Di Folco, E.; Chapillon, E.; Piétu, V. Impact of size-dependent grain temperature on gas-grain chemistry in protoplanetary disks: The case of low-mass star disks. *Astron. Astrophys.* **2021**, *654*, A65.

(20) Potapov, A.; McCoustra, M. Physics and chemistry on the surface of cosmic dust grains: a laboratory view. *International Reviews in Physical Chemistry* **2021**, *40*, 299–364.

(21) Potapov, A.; Jäger, C.; Henning, T. Temperature Programmed Desorption of Water Ice from the Surface of Amorphous Carbon and Silicate Grains as Related to Planet-forming Disks. *Astrophys. J.* **2018**, *865*, 58.

(22) Laffon, C.; Ferry, D.; Grauby, O.; Parent, P. Laboratory-based sticking coefficients for ices on a variety of small-grain analogues. *Nature Astronomy* **2021**, *5*, 445–450.

(23) Chirot, F.; Zamith, S.; Labastie, P.; L'Hermite, J.-M. New device to study unimolecular cluster nucleation. *Rev. Sci. Instrum.* **2006**, *77*, 063108.

(24) Braud, I.; Zamith, S.; L'Hermite, J.-M. A gas aggregation source for the production of heterogeneous molecular clusters. *Rev. Sci. Instrum.* **2017**, *88*, 043102.

(25) Holm, A. I. S.; Zettergren, H.; Johansson, H. A. B.; Seitz, F.; Rosén, S.; Schmidt, H. T.; Ławicki, A.; Rangama, J.; Rousseau, P.; Capron, M., et al. Ions Colliding with Cold Polycyclic Aromatic Hydrocarbon Clusters. *Phys. Rev. Lett.* **2010**, *105*, 213401.

(26) Rousseau, P.; Ławicki, A.; Holm, A.; Capron, M.; Maisonny, R.; Maclot, S.; Lattouf, E.; Johansson, H.; Seitz, F.; Méry, A., et al. Low-energy ions interacting with anthracene molecules and clusters. *Nucl. Instrum. Methods Phys. Res. B* **2012**, *279*, 140 – 143.

(27) West, B.; Useli-Bacchitta, F.; Sabbah, H.; Blanchet, V.; Bodi, A.; Mayer, P. M.; Joblin, C. Photodissociation of Pyrene Cations: Structure and Energetics from C16H10+ to C14+ and Almost Everything in Between. *J. Phys. Chem. A* **2014**, *118*, 7824–7831.

(28) Zhen, J.; Chen, T.; Tielens, A. G. G. M. Laboratory Photochemistry of Pyrene Clusters: An Efficient Way to Form Large PAHs. *Astrophys. J.* **2018**, *863*, 128.

(29) Mathur, B. P.; Field, J. E.; Colgate, S. O. Calculations of effusive-flow patterns. III. Scattering chambers with thin circular apertures. *Phys. Rev. A* **1975**, *11*, 830–.

(30) Zamith, S.; L'Hermite, J.-M.; Dontot, L.; Zheng, L.; Rapacioli, M.; Spiegelman, F.; Joblin, C. Threshold collision induced dissociation of pyrene cluster cations. *J. Chem. Phys.* **2020**, *153*, 054311.

(31) Armentrout, P. B.; Ervin, K. M.; Rodgers, M. T. Statistical Rate Theory and Kinetic Energy-Resolved Ion Chemistry: Theory and Applications. *J. Phys. Chem. A* **2008**, *112*, 10071–10085.

(32) Zamith, S.; Ji, M.-C.; L'Hermite, J.-M.; Joblin, C.; Dontot, L.; Rapacioli, M.; Spiegelman, F. Thermal evaporation of pyrene clusters. *J. Chem. Phys.* **2019**, *151*, 194303.

(33) Bondi, A. van der Waals Volumes and Radii. *J. Phys. Chem.* **1964**, *68*, 441–451.

(34) Langevin, P. Une formule fondamentale de théorie cinétique. *Ann. Chim. Phys.* **1905**, *5*, 245.

(35) Gioumousis, G.; Stevenson, D. P. Reactions of Gaseous Molecule Ions with Gaseous Molecules. V. Theory. *The Journal of Chemical Physics* **1958**, *29*, 294–299.

(36) Su, T.; Bowers, M. T. Ion-folar molecule collisions: the effect of ion size on ion-polar molecule rate constants; the parameterization of the average-dipole-orientation theory. *Intern. J. Mass Spectrom. Ion Phys.* **1973**, *12*, 347–356.

(37) Su, T.; Su, E. C. F.; Bowers, M. T. Ion–polar molecule collisions. Conservation of angular momentum in the average dipole orientation theory. The AADO theory. *J. Chem. Phys.* **1978**, *69*, 2243–2250.

(38) Su, T.; Bowers, M. T. Parameterization of the average dipole orientation theory: temperature dependence. *Intern. J. Mass Spectrom. Ion Phys.* **1975**, *17*, 211–212.

(39) Su, T.; Bowers, M. T. *Gas Phase Ion Chemistry*; Elsevier, 1979.

(40) Kummerlöwe, G.; Beyer, M. K. Rate estimates for collisions of ionic clusters with neutral reactant molecules. *Int. J. Mass Spectrom.* **2005**, *244*, 84–90.

(41) Dontot, L.; Spiegelman, F.; Rapacioli, M. Structures and Energetics of Neutral and Cationic Pyrene Clusters. *J. Phys. Chem. A* **2019**, *123*, 9531–9543.

(42) Dontot, L.; Spiegelman, F.; Zamith, S.; Rapacioli, M. Dependence upon charge of the vibrational spectra of small Polycyclic Aromatic Hydrocarbon clusters: the example of pyrene. *Eur. Phys. J. D* **2020**, *74*, 216.

(43) Attah, I. K.; Platt, S. P.; Meot-Ner (Mautner), M.; El-Shall, M. S.; Aziz, S. G.; Alyoubi, A. O. Hydrogen bonding of the naphthalene radical cation to water and methanol and attachment of the naphthalene ion to extended hydrogen bonding chains. *Chem. Phys. Lett.* **2014**, *613*, 45–53.

(44) Chatterjee, K.; Dopfer, O. Infrared spectroscopy of hydrated polycyclic aromatic hydrocarbon cations: naphthalene + water. *Phys. Chem. Chem. Phys.* **2017**, *19*, 32262–32271.

(45) Xu, B.; Stein, T.; Ablikim, U.; Jiang, L.; Hendrix, J.; Head-Gordon, M.; Ahmed, M. Probing solvation and reactivity in ionized polycyclic aromatic hydrocarbon–water clusters with photoionization mass spectrometry and electronic structure calculations. *Faraday Discuss.* **2019**, *217*, 414–433.

(46) Hernández-Rojas, J.; Calvo, F.; Rabilloud, F.; Bretón, J.; Gomez Llorente, J. M. Modeling Water Clusters on Cationic Carbonaceous Seeds. *J. Phys. Chem. A* **2010**, *114*, 7267–7274.

(47) Koizumi, H.; Armentrout, P. B. The kinetic energy dependence of association reactions. A new thermokinetic method for large systems. *The Journal of Chemical Physics* **2003**, *119*, 12819–12829.

(48) Joblin, C.; Dontot, L.; Garcia, G. A.; Spiegelman, F.; Rapacioli, M.; Nahon, L.; Parneix, P.; Pino, T.; Bréchignac, P. Size Effect in the Ionization Energy of PAH Clusters. *J. Phys. Chem. Lett.* **2017**, *8*, 3697–3702.

(49) Ulbricht, H.; Zacharia, R.; Cindir, N.; Hertel, T. Thermal desorption of gases and solvents from graphite and carbon nanotube surfaces. *Carbon* **2006**, *44*, 2931–2942.

(50) Bolina, A. S.; Wolff, A. J.; Brown, W. A. Reflection Absorption Infrared Spectroscopy and Temperature-Programmed Desorption Studies of the Adsorption and Desorption of Amorphous and Crystalline Water on a Graphite Surface. *The Journal of Physical Chemistry B* **2005**, *109*, 16836–16845.

(51) Joblin, C.; Toublanc, D.; Boissel, P.; Tielens, A. G. G. M. Calculations of the far-infrared emission of C 24 H 12 under interstellar conditions. *Molecular Physics* **2002**, *100*, 3595–3600.

(52) Mulas, G.; Malloci, G.; Joblin, C.; Toublanc, D. A general model for the identification of specific PAHs in the far-IR. *Astron. Astrophys.* **2006**, *460*, 93–104.

(53) Malloci, G.; Joblin, C.; Mulas, G. On-line database of the spectral properties of polycyclic aromatic hydrocarbons. *Chemical Physics* **2007**, *332*, 353–359.

(54) Beyer, T.; Swinehart, D. Algorithm 448: number of multiply-restricted partitions. *Communications of the ACM* **1973**, *16*, 379.

(55) Rapacioli, M.; Calvo, F.; Joblin, C.; Parneix, P.; Spiegelman, F. Vibrations and thermodynamics of clusters of polycyclic aromatic hydrocarbon molecules: The role of internal modes. *The Journal of Physical Chemistry A* **2007**, *111*, 2999–3009.

(56) Cernicharo, J. The Physical Conditions of Low Mass Star Forming Regions. The Physics of Star Formation and Early Stellar Evolution. 1991; p 287.

(57) Joblin, C.; Bron, E.; Pinto, C.; Pilleri, P.; Le Petit, F.; Gerin, M.; Le Bourlot, J.; Fuente, A.; Berne, O.; Goicoechea, J. R.; Habart, E., et al. Structure of photodissociation fronts in star-forming regions revealed by Herschel observations of high-J CO emission lines. *Astron. Astrophys.* **2018**, *615*, A129.

(58) Minissale, M.; Aikawa, Y.; Bergin, E.; Bertin, M.; Brown, W. A.; Cazaux, S.; Charnley, S. B.; Coutens, A.; Cuppen, H. M.; Guzman, V., et al. Thermal Desorption of Interstellar Ices: A Review on the Controlling Parameters and Their Implications from Snowlines to Chemical Complexity. *ACS Earth and Space Chemistry* **2022**, *6*, 597–630.

(59) Hensley, B. S.; Draine, B. T. Detection of PAH Absorption and Determination of the Mid-infrared Diffuse Interstellar Extinction Curve from the Sight Line toward Cyg OB2-12. *The Astrophysical Journal* **2020**, *895*, 38.

(60) Dontot, L.; Suaud, N.; Rapacioli, M.; Spiegelman, F. An extended DFTB-CI model for charge-transfer excited states in cationic molecular clusters: model studies versus ab initio calculations in small PAH clusters. *Phys. Chem. Chem. Phys.* **2016**, *18*, 3545–3557.

(61) Joblin, C.; Leger, A.; Martin, P. Contribution of Polycyclic Aromatic Hydrocarbon Molecules to the Interstellar Extinction Curve. *Astrophys. J. Lett.* **1992**, *393*, L79.

(62) Chakraborty, P.; Zachariah, M. R. Sticking Coefficient and Processing of Water Vapor on Organic-Coated Nanoaerosols. *J. Phys. Chem. A* **2008**, *112*, 966–972.

(63) Marciante, M.; Calvo, F. Communication: Nucleation of water on ice nanograins: Size, charge, and quantum effects. *J. Chem. Phys.* **2015**, *142*, 171104.

(64) Lange, K.; Dominik, C.; Tielens, A. G. G. M. Stability of polycyclic aromatic hydrocarbon clusters in protoplanetary discs. *Astron. Astrophys.* **2021**, *653*, A21.

(65) Kamp, I.; Thi, W. F.; Woitke, P.; Rab, C.; Bouma, S.; Ménard, F. Consistent dust and gas models for protoplanetary disks. II. Chemical networks and rates. *Astron. Astrophys.* **2017**, *607*, A41.

(66) Pilleri, P.; Joblin, C.; Boulanger, F.; Onaka, T. Mixed aliphatic and aromatic composition of evaporating very small grains in NGC 7023 revealed by the 3.4/3.3 μm ratio. *Astron. Astrophys.* **2015**, *577*, A16.

(67) Boutéraon, T.; Habart, E.; Ysard, N.; Jones, A. P.; Dartois, E.; Pino, T. Carbonaceous nano-dust emission in proto-planetary discs: the aliphatic-aromatic components. *Astron. Astrophys.* **2019**, *623*, A135.

(68) Ballering, N. P.; Cleeves, L. I.; Anderson, D. E. Simulating Observations of Ices in Protoplanetary Disks. *Astrophys. J.* **2021**, *920*, 115.

Graphical TOC Entry

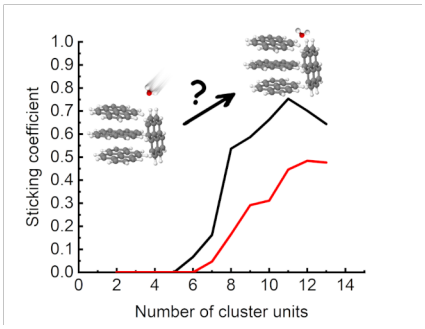

For Table of Contents Only